



## Momentum-transfer-dependence behavior of the 3s autoionization resonances of argon studied by high-resolution fast electron scattering

Xiao-Jiao Du, Yuan-Chen Xu, Li-Han Wang , Tian-Jun Li, Zi-Ru Ma, Shu-Xing Wang\*, and Lin-Fan Zhu <sup>†</sup>

Hefei National Laboratory for Physical Sciences at Microscale and Department of Modern Physics, University of Science and Technology of China, Hefei, Anhui 230026, People's Republic of China



(Received 31 August 2021; accepted 4 January 2022; published 18 January 2022)

The asymmetric Fano profile, which is caused by the two-channel interference between discrete states and relevant continuum states, presents a great challenge to atomic and molecular physics. This study investigates the inner-valence excitations of argon 3s electrons in the energy range 24.5–29.5 eV using an electron energy-loss spectrometer. The absolute generalized oscillator strength densities of the 3s excitations and the Fano profile parameters (i.e.,  $q$ ,  $f_a$ ,  $\rho^2$ ,  $f$ ,  $S$ ) in  $0 < K^2 < 2.2$  a.u. for the  $3s3p^6ns$  ( $n = 4$  and  $5$ ),  $3s3p^6np$  ( $n = 4$  and  $5$ ), and  $3s3p^63d$  autoionization states are determined. For the same Rydberg series, similar momentum-transfer-dependence behaviors are observed for the Fano profile parameters  $q$ ,  $f_a$ ,  $\rho^2$ ,  $f$ , and  $S$ . The magnitudes of  $q$  and  $f_a$  are found to be nearly equal for the same Rydberg series, while the corresponding  $f$  and  $S$  parameters decrease as the principal quantum number increases, confirming the theoretical predictions of Fano and Cooper [U. Fano and J. W. Cooper, *Phys. Rev.* **137**, A1364 (1965)]. Moreover, the typical dipole-allowed or dipole-forbidden  $K^2$ -dependence behaviors of the Fano profile parameters are used to elucidate the properties of electric transition multipolarities. The parameters of the Fano profile derived in a large  $K^2$  region offer an opportunity to understand the wave functions far away from the nucleus.

DOI: [10.1103/PhysRevA.105.012812](https://doi.org/10.1103/PhysRevA.105.012812)

### I. INTRODUCTION

Autoionization states, involving strong electron correlation effects and configuration interactions, were first observed by Beutler [1] in the photoabsorption spectra of noble gas atoms. The characterized asymmetric resonance profiles have attracted widespread attention both experimentally and theoretically. Since Fano first proposed the theoretical explanation of the asymmetric line profiles and parametrized the interference effect in the 1960s [2–4], numerous studies have probed the physical properties of the autoionization states. The inherent physical complexity of the observed phenomena can be expressed by a few parameters since then. Nowadays, Fano resonance has been introduced to many fields besides atomic and molecular physics to interpret the observed interference phenomena between two interacting quantum channels, such as in condensed-matter physics and nanostructures [5,6]. Moreover, the doubly excited states of helium are of particular interest because it is the simplest two-electron system [7–13]. The inner-valence excitations of heavier noble atoms have also been extensively studied using the synchrotron radiations or the short-pulse lasers [7,12–21].

Initially, most studies on the asymmetric Fano autoionization resonances focused on the energy levels, profile parameters, photoionization cross sections, and their decay processes. With the development of laser technology, in particular, the generation of attosecond laser pulses, the time-resolved

photoionization process began to be examined [12–14]. Note that a universal temporal-phase formalism can map the Fano asymmetry parameter  $q$  to a phase of the time-dependent dipole response function [12]. This result leads directly to the transformation of a Fano profile into a naturally Lorentzian line and vice versa. The abovementioned studies motivate us to develop deeper insights into the autoionization resonance. However, optical methods are usually limited by the selection rules for dipole-allowed transitions [22,23]. The fast electron impact method based on the electron energy-loss spectrometer is capable of studying the dipole-forbidden excitations as well as the momentum-transfer-dependence behaviors. For example, the double-excitation processes of one strong dipole-allowed series [ ${}_n(0, 1)_2^+ 1P^o$ ] and two weak dipole-forbidden series [ ${}_n(1, 0)_2^+ 1S^e$  and  ${}_n(1, 0)_2^+ 1D^e$ ] of helium have been studied using a high-resolution fast-electron energy-loss spectrometer [10]. Subsequently, Yuan *et al.* [11] performed the corresponding theoretical calculations with the  $R$ -matrix method to enable a comparison with the experimental results.

As a noble gas atom with a compact closed-shell system, argon constitutes an ideal target for testing and developing theoretical models. The inner-valence excited states  $3s3p^6np$  of argon were first identified in the photoabsorption spectrum by Madden and Codling [7]. With the development of the different experimental techniques and improvements in the measurement instruments, the energy levels of the autoionization resonances of argon have been extensively investigated. The resonance positions and natural linewidths of the inner 3s electron excitations have been comprehensively studied, including both the dipole-allowed and the dipole-forbidden

\*wangshuxing@ustc.edu.cn

<sup>†</sup>lfzhu@ustc.edu.cn

transitions. Most experimental work used the photoabsorption technique and electron or ion impact method [18,19,21,24–40], in which the particle impact methods have obvious advantages in observing the dipole-forbidden autoionization states. Measurements with low-incident electron energies concentrated mainly on the energy levels, the triplet-singlet separation, and postcollision interactions [24–27]. Comprehensive analysis of the resonance levels of autoionization states obtained using low-energy heavy-ion impacts has been reported by Jorgensen *et al.* [28], and the observed energy levels have been assigned using molecular-orbital diagrams and the Wigner spin conservation rule. Jorgensen *et al.* [28] found that variations in the atomic number or charge state of the projectile produced considerable changes in the spectra.

In this study, we investigate the Fano profile parameters of the inner-valence excitations and the momentum-transfer-dependence behaviors. Accurate cross sections and profile parameters of the Fano autoionization resonance are essential for analyzing the configuration interactions involving the relevant discrete and continuum states. The photoabsorption cross sections of argon  $3s$  autoionization states have previously been established using the optical absorption methods [17–20], but these may produce certain errors due to the line saturation effects that occur when the experimental resolution is wider than the natural linewidth [17,18,37]. Additionally, the photoionization cross sections of argon in the energy range 25.0–29.3 eV have been reported by Sorensen *et al.* [21], who used the synchrotron-radiation-excited ion mass spectrometry. In Refs. [19,21], the Fano parameters were determined by fitting the Fano profiles of  $3s3p^6np$  resonances of argon. Unlike the photoabsorption methods, electron impact techniques are free from the line saturation effects. The absolute optical oscillator strength densities (or photoabsorption cross sections) of the  $3s3p^6np$  autoionization resonances of argon have been determined by the dipole ( $e, e$ ) method with incident electron energies of 3 and 2.5 keV at an average scattering angle of  $0^\circ$  [37,38]. Moreover, the fitted Fano profile parameters reported by Wu *et al.* [38] can be used for comparative analysis with the optical results.

Note that the autoionization states have been extensively studied by the photoabsorption and dipole ( $e, e$ ) methods for cases where the momentum transfer was negligibly small. It is well known that oscillator strength at small momentum transfers reflects the properties of the wave function far from the nucleus. The measurements achieved by fast electron scattering can cover a large  $K^2$  region, reflecting the information of the wave functions both far from and close to the nucleus [10]. Under the experimental condition of high-impact electron energies and large scattering angles, the profile parameters of asymmetric Fano resonance for the optically forbidden excitations of argon  $3s$  electrons have been determined by Zhu *et al.* [39]. The dependence behaviors of the autoionization profile parameters of argon on the incident electron energies and scattering angles have been performed using the low-energy electron impact [27,36]. In particular, Ref. [27] defined new parameters through the numerical transformation of the Fano parameters, enabling a more convenient description of the line shapes and intensities of the measured autoionization resonances spectra. Note that the first Born approximation does not apply in the case of low-energy impacts. On the

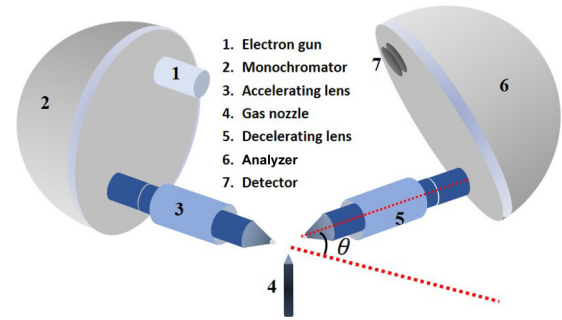


FIG. 1. Schematic diagram of present electron energy-loss spectrometer

theoretical side, the energy levels of the autoionization states of argon have been predicted based on the quantum number defect [32] and through Rydberg-Ritz analysis [25]. The Fano profile parameters of some dipole-allowed autoionization resonances of argon have been reported using the  $R$ -matrix and multichannel multiconfiguration Dirac-Fock methods [21,41]. Additionally, the energy-loss spectra of high-energy electrons incident on an argon atom have been investigated using linear density response theory with a self-interaction correction [42,43], where the momentum-transfer-dependence behaviors of the fitted line shape index  $q$  were determined for the  $3s3p^64p$  and  $3s3p^64d$  autoionization states.

This paper describes measurements of electron energy-loss spectra in the range 24.5–29.5 eV at an incident electron energy of 1.5 keV with an energy resolution of about 80 meV, including the autoionization states  $3s3p^6ns$  ( $n = 4–7$ ),  $3s3p^6np$  ( $n = 4–7$ ), and  $3s3p^6nd$  ( $n = 3–5$ ). The measured spectra are fitted using the Fano formula, and the Fano profile parameters are obtained for the well-resolved  $3s3p^6ns$  ( $n = 4$  and  $5$ ),  $3s3p^6np$  ( $n = 4$  and  $5$ ), and  $3s3p^63d$  states as a function of the momentum transfers. We report the similarities and differences between the profiles parameters for the same Rydberg series. The  $K^2$ -dependence behaviors of all the parameters of the electric multipole transitions are discussed carefully. The remainder of this paper is organized as follows. In Sec. II, we briefly describe the experimental method and data analysis. The experimental results are presented and compared with the available experimental and theoretical data in Sec. III. Finally, we summarize the conclusions to the present work in Sec. IV.

## II. EXPERIMENT AND DATA ANALYSIS

The measurements were carried out at a high-resolution fast-electron energy-loss spectrometer (EELS) [38,44,45] operated at an incident electron energy of 1.5 keV and an energy resolution of about 80 meV. Figure 1 shows a schematic diagram of the EELS. Briefly, the apparatus consists of an electron gun, a hemispherical electrostatic monochromator, a rotatable energy analyzer, several cylindrical electrostatic optics lenses, and a position-sensitive detector based on microchannel plates. All of these components are enclosed in three separate vacuum chambers made of stainless steel, with the differential pumping ensuring the operational stability of the spectrometer. Crossed beams were adopted for the present

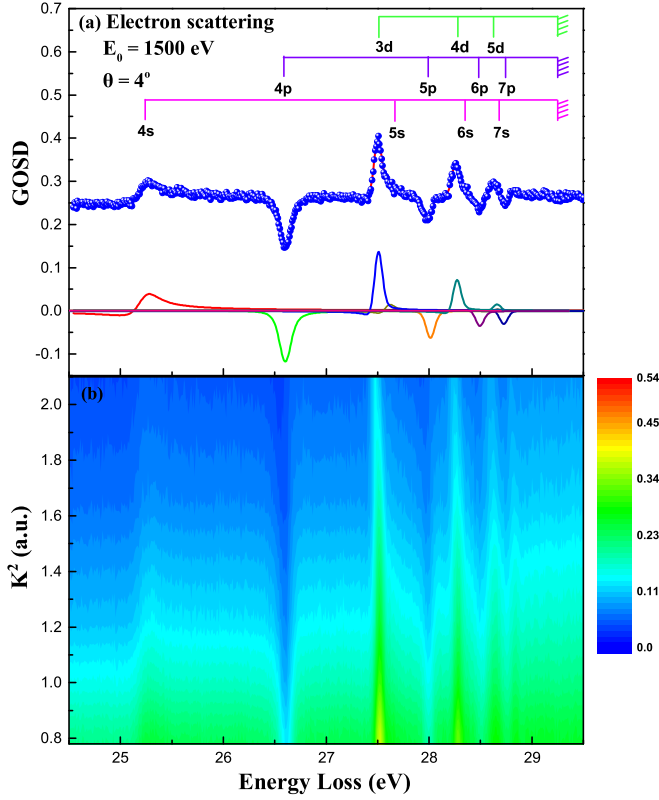


FIG. 2. (a) Absolute GOSD of the autoionization states of argon at a scattering angle of  $4^\circ$ . The curves are the fitted results. (b) A 2D map of the GOSD of argon vs the energy loss and squared momentum transfer measured by the present high-energy electron scattering.

experiments, whereby the electrons collided with the sample gases diffused from a gas nozzle in the interaction chamber. The background and operating pressures were  $5 \times 10^{-5}$  and  $2 \times 10^{-3}$  Pa, respectively.

In this work, experimental spectra were recorded in the energy ranges 11–14 and 24–30 eV at scattering angles of  $2^\circ$ – $8^\circ$ . The generalized oscillator strength (GOS) of the  $3p^6 \ ^1S_0 \rightarrow 3p^5 4s' \ [1/2]_1$  transition was used to normalize the ionization continuum in which the autoionization states are located. The GOS of the valence-shell excited state  $3p^5 4s' \ [1/2]_1$  has been reported in detail by Chen *et al.* [46]. A typical GOS density (GOSD) spectrum at a scattering angle of  $4^\circ$  is depicted in Fig. 2(a). A two-dimensional (2D) map for the GOSD of the  $3s$  autoionization states of argon is shown in Fig. 2(b). The GOSDs of the autoionization states measured at some selected angles with different flow rates coincide with each other within the experimental uncertainties, indicating that the present measurements are free from the pressure effect [44,47,48].

Within the FBA, the GOS (whose properties play central roles in the collisions of fast charged particles with atoms and molecules) was introduced by Bethe [49,50]. Later, Inokuti [51] generalized the GOS to describe the continuum as

$$\frac{df}{dE} = \sum_n \frac{2E_n}{K^2} \left| \langle \Psi_{n,E} | \sum_{j=1}^N e^{i\mathbf{K}\cdot\mathbf{r}_j} | \Psi_0 \rangle \right|^2 \delta(E_n - E). \quad (1)$$

Here  $\frac{df}{dE}$  is the GOSD at an energy loss of  $E$ , while  $\Psi_0$  and  $\Psi_{n,E}$  are the  $N$ -electron wave functions for the initial and final (continuum) states, respectively.  $E_n$  is the excitation energy, and  $\delta(E_n - E)$  denotes the energy conservation.  $\mathbf{K}$  is the momentum transfer vector, and  $\mathbf{r}_j$  is the position vector of the  $j$ th electron. The summation is over all channels of the final states.

According to Fano's theory, the GOSD of the autoionization resonance can be written as

$$\begin{aligned} \frac{df}{dE} &= \sum_i f_{ai} [q_i \sin \Delta_i - \cos \Delta_i]^2 - 1 + f_c(E) \\ &= \sum_i f_{ai} \left( \frac{(q_i + \varepsilon_i)^2}{1 + \varepsilon_i^2} - 1 \right) + f_c(E) \\ &= f_c(E) \left[ \sum_i \rho_i^2 \left( \frac{q_i^2 - 1 + 2q_i \varepsilon_i}{1 + \varepsilon_i^2} \right) + 1 \right], \quad (2) \end{aligned}$$

where  $f_{ai}$  represents the GOSD of the relevant continuum states involving the interference with the  $i$ th resonance.  $f_c(E)$  is the total continuum GOSD, which includes both parts that do and do not interfere with the resonance.  $\Delta_i$  is the phase shift due to the configuration interactions.  $\varepsilon_i = -\cot \Delta_i = (E - E_{ri})/(\Gamma_i/2)$ , which describes the deviation of the excitation energy  $E$  from an idealized resonance energy  $E_{ri}$  scaled by the linewidth  $\Gamma_i$ .  $\Gamma_i = 2\pi |V_E|^2$ , where  $V_E$  is the discrete-continuum interactions matrix element.  $q_i$  is a numerical index that characterizes the line profile.

In the final form of Eq. (2), the term proportional to  $q_i^2$  represents the intrinsic Lorentz profile of an autoionization state, unaffected by interference. The next term, with a coefficient of  $-1$ , depicts the effect of spectral repulsion and the third term describes the interference effect [4].

The parameter  $q_i$  can be described as

$$q_i = \frac{(\Psi_i | T | \Psi_0)}{\pi V_E^* (\Psi_E | T | \Psi_0)}, \quad (3)$$

where  $\Psi_i$  is the  $i$ th "modified" discrete state.  $\Psi_E$  is the unperturbed continuum state, which can interact with the discrete resonance.  $T = \sum_j e^{i\mathbf{K}\cdot\mathbf{r}_j}$  is the transition operator. Therefore,  $q_i$  reflects the ratio of the scattering amplitudes from the initial state to the modified discrete state  $\Psi_i$  and to the unperturbed continuum state  $\Psi_E$  [2].

The parameter  $\rho_i^2$ , which describes the proportion of the continuum that interacts with the  $i$ th autoionizing state, is defined as

$$\rho_i^2 = \frac{f_{ai}(K, E)}{f_c(K, E)} \Big|_{E=E_{ri}}. \quad (4)$$

For a specific resonance, the integrated GOS  $f_i$  of the modified embedded discrete state can be expressed as [2]

$$f_i = \int f_{ai} q_i^2 \sin^2 \Delta_i dE = \frac{\pi \Gamma_i}{2} f_{ai} q_i^2 \Big|_{E=E_{ri}}. \quad (5)$$

Furthermore, an integrated resonance strength  $S_i$  is introduced to represent the relevant strength involving interference between the embedded discrete state and the relevant continuum

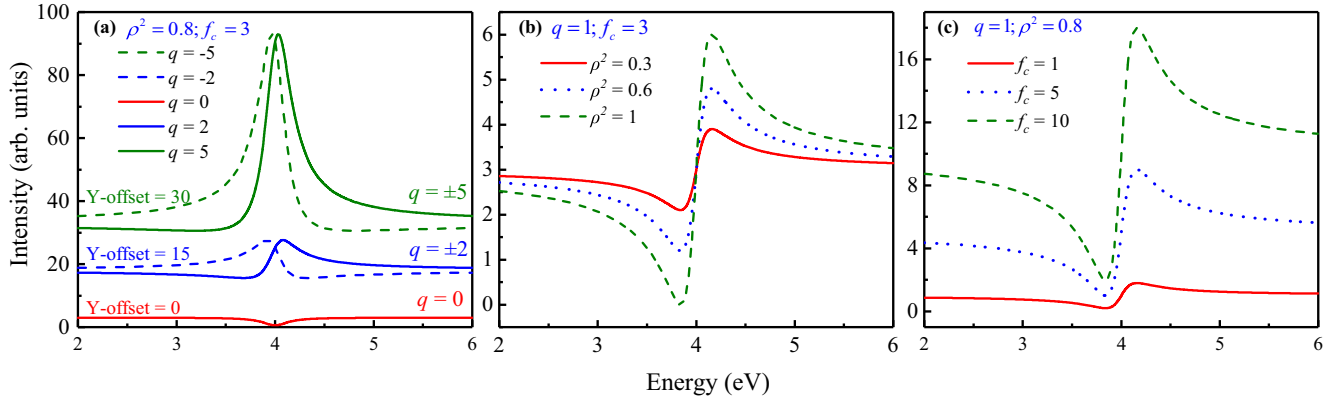


FIG. 3. Numerical simulation for the Fano profile at a resonance energy  $E_r$  of 4 eV and a natural width  $\Gamma$  of 0.08 eV. (a) Fano profiles with the various values of the asymmetry factor  $q$ . (b) Fano profiles with various values of the ratio parameter  $\rho^2$ . (c) Fano profiles with various values of the total continuum  $f_c$ .

as a whole [10,11]:

$$S_i = f_i + \frac{\pi \Gamma_i}{2} f_{ai} \Big|_{E=E_{ri}} = \frac{\pi \Gamma_i}{2} (q_i^2 + 1) f_{ai} \Big|_{E=E_{ri}}. \quad (6)$$

To clarify the roles of these parameters in fitting the Fano profiles, the numerical results for the Fano resonance with different profile parameters are shown in Fig. 3. The simulations used the final form of Eq. (2) at a resonance energy  $E_r$  of 4 eV and a natural width  $\Gamma$  of 0.08 eV.

Experimentally, it is challenging to obtain reliable Fano profile parameters due to the heavy overlap between different Rydberg states. The key to obtaining reliable experimental results is to reduce the number of related variables during data fitting. In the present work, a least-squares fitting was used to fit the experimental spectra. The profile parameters of the  $3s3p^6np$  ( $n = 4$  and 5),  $3s3p^6ns$  ( $n = 4$  and 5), and  $3s3p^63d$  states were obtained. In the following, these inner-valence excited states are abbreviated as  $3s^{-1}nl$  for convenience. In the fitting procedure, the Fano profiles were convoluted with a Gaussian function to represent the instrumental function. The Gaussian linewidth was obtained by fitting the valence-shell excited state  $3p^54s'[1/2]_1$  with a narrow natural linewidth. Note that  $\rho^2$  should be identical for the same Rydberg series [3,19,38]. The autoionization resonances have uniform natural linewidths at different scattering angles. The profile parameters, including the resonance energy  $E_r$ , the natural width  $\Gamma$ , the asymmetry parameter  $q$ ,  $\rho^2$ , and  $f_c$ , were obtained with the shared  $\rho^2$  and locked  $\Gamma$  and  $E_r$  reported in Refs. [38,39]. The experimental errors in this work are estimated to be about 5–30%, including the contributions from the finite angular resolution, the angle determination, the statistical counts, the least-squares fitting, and the normalizing procedure. The total experimental errors are shown in the corresponding figures.

### III. RESULTS AND DISCUSSION

To compare the behaviors of the Fano profile parameters, the asymmetry factor  $q$ , the ratio parameter  $\rho^2$ , the interfering continuum  $f_a$ , the integrated GOS  $f$ , and the resonance strength  $S$  are shown in Figs. 4–8 for the electric dipole transitions to the  $3s^{-1}np$  ( $n = 4$  and 5) states, the electric

monopole transitions to the  $3s^{-1}ns$  ( $n = 4$  and 5) states, and the electric quadrupole transition to the  $3s^{-1}3d$  state. For comparison with the present experimental results, previous measured and calculated data are also collected and presented in the corresponding figures.

The asymmetry factor  $q$  of the associated resonances is presented in Fig. 4. The same  $q$  values and  $K^2$  dependence behaviors in the same Rydberg series are found for the  $3s^{-1}np$  ( $n = 4$  and 5) and  $3s^{-1}ns$  ( $n = 4$  and 5) states. The minor discrepancies can be attributed to experimental errors and the heavy overlap between the  $3s^{-1}5s$  and  $3s^{-1}3d$  states. For the electric dipole transitions, the  $q$  factor increases monotonically from negative to positive with increasing  $K^2$ , demonstrating that the resonance varies from constructive interference to destructive interference in the low-energy wing,

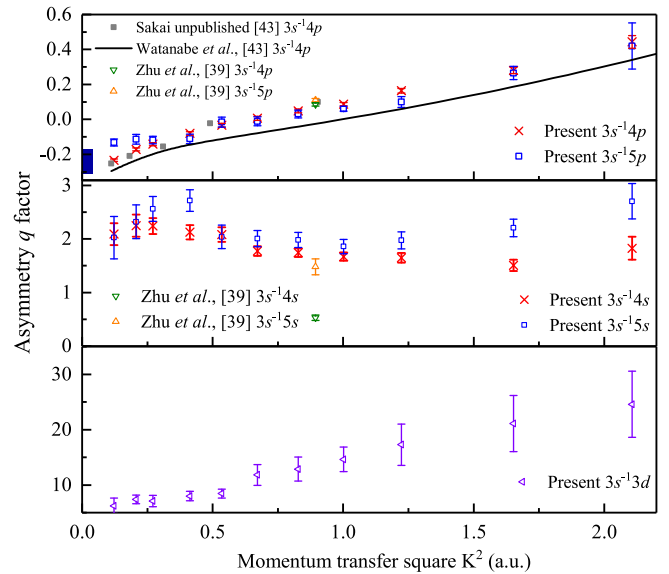


FIG. 4. Fano profile index  $q$  of the  $3s^{-1}ns$  ( $n = 4$  and 5),  $3s^{-1}np$  ( $n = 4$  and 5), and  $3s^{-1}3d$  resonances of argon as a function of  $K^2$ . The column bar near the  $y$  axis indicates the range of  $q$  values of the photoabsorption [19,21] and dipole ( $e, e$ ) [38] measurements and the  $R$ -matrix calculation [41].



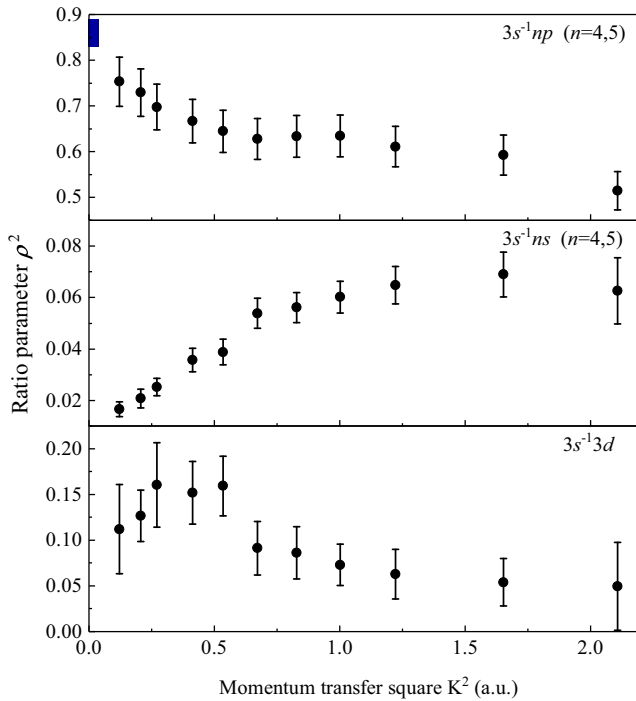


FIG. 5. Ratio parameter  $\rho^2$  of the  $3s^{-1}ns$  ( $n = 4$  and  $5$ ),  $3s^{-1}np$  ( $n = 4$  and  $5$ ), and  $3s^{-1}3d$  resonances of argon as a function of  $K^2$ . The column bar near the y axis indicates the range of  $\rho^2$  of the photoabsorption [19,21] and dipole ( $e, e$ ) [38] measurements and the  $R$ -matrix calculation [41].

while the reverse behavior occurs in the high-energy wing. At  $K^2 \approx 0.67$  a.u., typical window resonance (i.e.,  $q = 0$ ) can be observed for the  $3s^{-1}np$  ( $n = 4$  and  $5$ ) states, indicating that the transition probability to the modified discrete state is zero. Moreover, most of the available experimental and theoretical data are in agreement with the present results, while the calculations reported by Watanabe *et al.* [43] are slightly lower than the experimental data. This discrepancy is caused by the high-order interactions being neglected [42,43]. The observed  $q$  factor of the monopole transition shows an oscillation within the present  $K^2$  region. The only available previous data of Zhu *et al.* [39] are lower than the present results. One possible explanation is that the previous fitting procedure did not handle the multiresonance spectra sufficiently well, particularly for the heavily overlapped structures. Thus, there is an obvious difference between the present  $q$  value and the previous one [39] for the  $3s^{-1}5s$  state, which is close to that for the  $3s^{-1}3d$  state. The observed  $q$  factor for the quadrupole transition increases from a minimum of 6.24 to a maximum of 24.57. A higher  $q$  value implies a near-symmetric line profile and weak interference.

The ratio parameter  $\rho^2$ , which indicates the fraction of the continuum that interacts with the autoionizing state, was treated as a shared parameter for the same Rydberg series in the fitting procedure [3,19,38]. As shown in Fig. 5,  $\rho^2$  is much lower for the dipole-forbidden transitions than for the electric dipole transitions. Furthermore, for the electric dipole transitions,  $\rho^2$  decreases with increasing  $K^2$ , showing the typical dipole-allowed behavior. This is reasonable

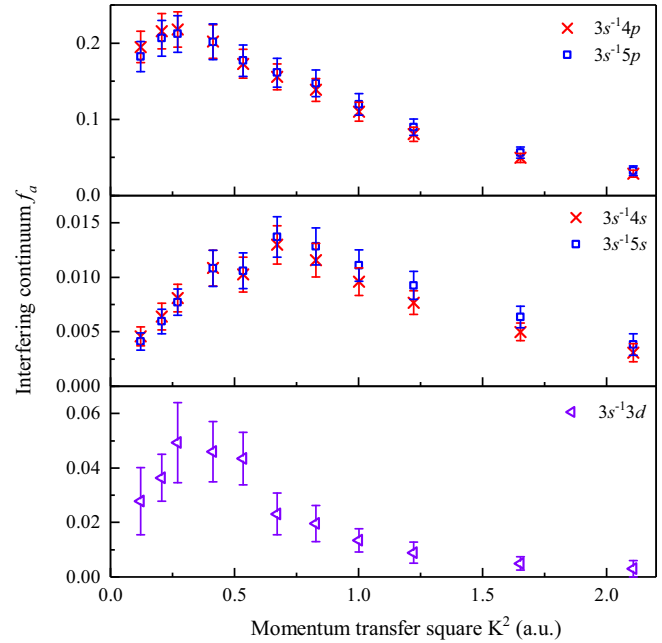


FIG. 6. Interfering continuum  $f_a$  of the  $3s^{-1}ns$  ( $n = 4$  and  $5$ ),  $3s^{-1}np$  ( $n = 4$  and  $5$ ), and  $3s^{-1}3d$  resonances of argon as a function of  $K^2$ .

because the dipole-allowed transition dominates at  $K^2 = 0$ , while the components of the dipole-forbidden transitions will be highlighted as  $K^2$  increases. At  $K^2 = 0$ , the maximum is obtained by electron impact [38] and photoabsorption experiments [19,21], as well as in the theoretical calculations [41], in agreement with the tendency of the fitted data points. In addition, for the electric monopole and quadrupole transitions,

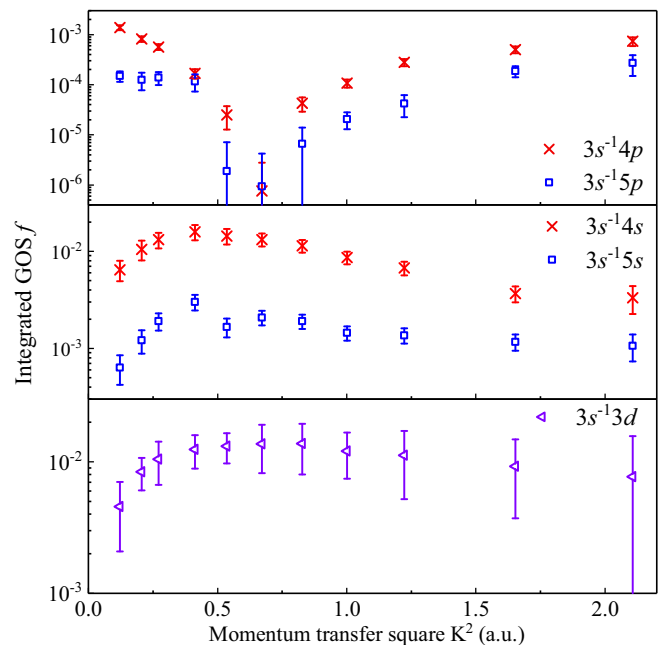


FIG. 7. Integrated GOS  $f$  of the  $3s^{-1}ns$  ( $n = 4$  and  $5$ ),  $3s^{-1}np$  ( $n = 4$  and  $5$ ), and  $3s^{-1}3d$  resonances of argon as a function of  $K^2$ .

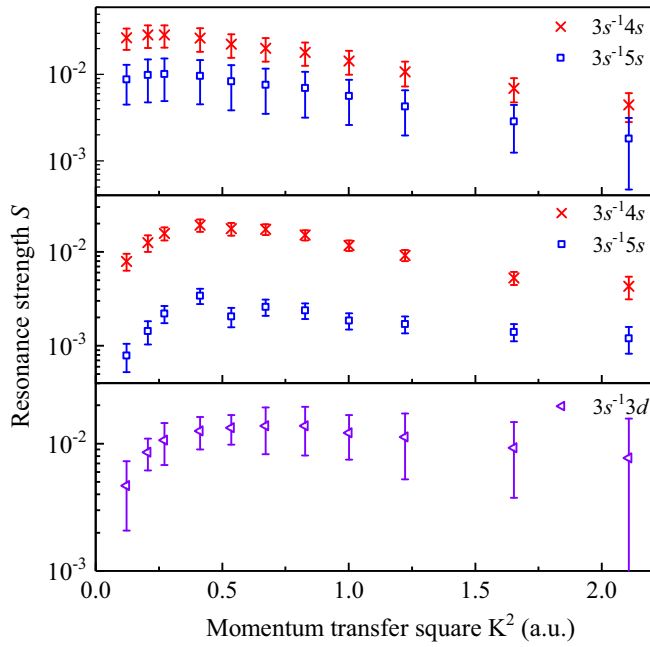


FIG. 8. Resonance strength  $S$  of the  $3s^{-1}ns$  ( $n = 4$  and  $5$ ),  $3s^{-1}np$  ( $n = 4$  and  $5$ ), and  $3s^{-1}3d$  resonances of argon as a function of  $K^2$ .

$\rho^2$  exhibits typical dipole-forbidden behavior, i.e., the ratio increases at first and then decreases with  $K^2$ . The interfering continuum  $f_a$  is presented in Fig. 6. Although  $f_a$  features similar behavior for the different transitions, extrapolating  $f_a$  to the limit of zero squared momentum transfer suggests that the values for the electric monopole and quadrupole transitions are close to zero, whereas the value for the electric dipole is about 0.13. This agrees with the typical dipole-forbidden and dipole-allowed behaviors. Moreover, the fitted  $f_a$  and their  $K^2$ -dependence behaviors for the same Rydberg series are also in good agreement, which supports the theoretical expectation [3].

The integrated GOS is the most widely used parameter in EELS experiments. However, the integrated GOS  $f$  for an autoionizing resonance vanishes when  $q = 0$ , i.e., the destructive interference reaches a maximum for window resonance. Thus, an integrated resonance strength was introduced to describe the relevant strength involving interference between the embedded discrete state and the relevant continuum as a whole [10,11]. The fitted integrated GOS  $f$  and the resonance strength  $S$  for the associated resonances are shown in Figs. 7 and 8. A similar  $K^2$ -dependence behavior for the same Ryd-

berg series can be observed for  $f$  and  $S$ . Fano and Cooper [3] stated that the natural linewidths for the  $3s^{-1}nl$  states are approximately inversely proportional to  $n^3$ . Therefore, the associated GOS  $f$  and resonance strength  $S$  for the  $3s^{-1}4p$  and  $3s^{-1}4s$  states are higher than those of the  $3s^{-1}5p$  and  $3s^{-1}5s$  states. For the electric dipole Rydberg states, the integrated GOS  $f$  experiences a sharp decline to a minimum of zero at  $K^2 \approx 0.67$  a.u. and then rises as  $K^2$  increases, showing the typical behavior of dipole-allowed transitions. As  $|q|$  is quite small for the dipole transitions, the  $K^2$ -dependence behavior of the resonance strength  $S$  relies more on the relevant continuum  $f_a$ . With regard to the monopole and quadrupole transitions with large  $q$  factors, the  $K^2$ -dependent behaviors of the integrated GOS  $f$  and the resonance strength  $S$  are inevitably consistent. Furthermore,  $f$  and  $S$  as a function of  $K^2$  manifest the typical dipole-forbidden behaviors.

#### IV. SUMMARY AND CONCLUSION

In conclusion, the absolute GOSD of the inner-valence  $3s$  electron excitations of argon has been determined at an incident electron energy of 1500 eV. The Fano profile parameters of the  $3s^{-1}np$  ( $n = 4$  and  $5$ ),  $3s^{-1}ns$  ( $n = 4$  and  $5$ ), and  $3s^{-1}3d$  autoionization states are obtained by least-squares fitting and are generally in good agreement with previous experimental measurements and theoretical calculations. The fitted  $q$  and  $f_a$  of the autoionization states  $3s^{-1}nl$  are independent with the principal quantum number  $n$ , whereas  $f$  and  $S$  decrease with  $n$ , which agrees with the theoretical predictions [3]. Furthermore, the profile parameters in a Rydberg series feature similar  $K^2$ -dependence behaviors. The momentum-transfer-dependence behaviors of the Fano profile parameters  $\rho^2$ ,  $f_a$ ,  $f$ , and  $S$  are observed to feature the typical behaviors of the dipole-allowed or dipole-forbidden transitions, and thus they can serve as a reference for distinguishing the electric transition multiplicities. The Fano profile parameters reported in this paper for the  $3s$  autoionization resonances of argon in a large  $K^2$  region provide more complete information of the corresponding wave functions both far from and close to the nucleus. Furthermore, the present experimental data can serve as a testing benchmark for future theoretical investigations.

#### ACKNOWLEDGMENTS

This work was supported by the National Natural Science Foundation of China (Grant No. U1932207) and the National Key Research and Development Program of China (Grants No. 2017YFA0402300 and No. 2017YFA0303500). The authors would also like to thank the Heavy Ion Research Facility in Lanzhou (HIRFL) for financial support.

- [1] H. Beutler, *Z. Phys.* **93**, 177 (1935).
- [2] U. Fano, *Phys. Rev.* **124**, 1866 (1961).
- [3] U. Fano and J. W. Cooper, *Phys. Rev.* **137**, A1364 (1965).
- [4] U. Fano and J. W. Cooper, *Rev. Mod. Phys.* **40**, 441 (1968).
- [5] A. E. Miroshnichenko, S. Flach, and Y. S. Kivshar, *Rev. Mod. Phys.* **82**, 2257 (2010).

- [6] K. P. Heeg, C. Ott, D. Schumacher, H. C. Wille, R. Röhlberger, T. Pfeifer, and J. Evers, *Phys. Rev. Lett.* **114**, 207401 (2015).
- [7] R. P. Madden and K. Codling, *Phys. Rev. Lett.* **10**, 516 (1963).
- [8] M. Domke, G. Remmers, and G. Kaindl, *Phys. Rev. Lett.* **69**, 1171 (1992).
- [9] G. Tanner, K. Richter, and J. M. Rost, *Rev. Mod. Phys.* **72**, 497 (2000).

- [10] X. J. Liu, L. F. Zhu, Z. S. Yuan, W. B. Li, H. D. Cheng, Y. P. Huang, Z. P. Zhong, K. Z. Xu, and J. M. Li, *Phys. Rev. Lett.* **91**, 193203 (2003).
- [11] Z. S. Yuan, X. Y. Han, X. J. Liu, L. F. Zhu, K. Z. Xu, L. Voky, and J. M. Li, *Phys. Rev. A* **70**, 062706 (2004).
- [12] C. Ott, A. Kaldun, P. Raith, K. Meyer, M. Laux, J. Evers, C. H. Keitel, C. H. Greene, and T. Pfeifer, *Science* **340**, 716 (2013).
- [13] C. Ott, L. Aufleger, T. Ding, M. Rebholz, A. Magunia, M. Hartmann, V. Stooß, D. Wachs, P. Birk, G. D. Borisova, K. Meyer, P. Rupprecht, C. da Costa Castanheira, R. Moshhammer, A. R. Attar, T. Gaumnitz, Z. H. Loh, S. Düsterer, R. Treusch, J. Ullrich *et al.*, *Phys. Rev. Lett.* **123**, 163201 (2019).
- [14] H. Wang, M. Chini, S. Y. Chen, C. H. Zhang, F. He, Y. Cheng, Y. Wu, U. Thumm, and Z. Chang, *Phys. Rev. Lett.* **105**, 143002 (2010).
- [15] K. Schulz, M. Domke, R. Püttner, A. Gutiérrez, G. Kaindl, G. Miecznik, and C. H. Greene, *Phys. Rev. A* **54**, 3095 (1996).
- [16] D. L. Ederer, *Phys. Rev. A* **4**, 2263 (1971).
- [17] J. A. R. Samson, *Phys. Rev.* **132**, 2122 (1963).
- [18] J. A. R. Samson, *Adv. At. Mol. Phys.* **2**, 177 (1966).
- [19] R. P. Madden, D. L. Ederer, and K. Codling, *Phys. Rev.* **177**, 136 (1969).
- [20] R. W. Carlson, D. L. Judge, M. Ogawa, and L. C. Lee, *Appl. Opt.* **12**, 409\_1 (1973).
- [21] S. L. Sorensen, T. Åberg, J. Tulkki, E. Rachlew-Källne, G. Sundström, and M. Kirm, *Phys. Rev. A* **50**, 1218 (1994).
- [22] L. F. Zhu, H. C. Tian, Y. W. Liu, K. Yang, and G. X. Liu, *Chin. Phys. B.* **24**, 043101 (2015).
- [23] H. C. Tian, L. Q. Xu, and L. F. Zhu, *Chin. Phys. B.* **27**, 043101 (2018).
- [24] E. Bolduc, J. J. Quémener, and P. Marmet, *Can. J. Phys.* **49**, 3095 (1971).
- [25] J. Fryar and J. W. McConkey, *J. Phys. B: At., Mol. Opt. Phys.* **9**, 619 (1976).
- [26] D. G. Wilden, J. Comer, and P. J. Hicks, *Nature (London)* **273**, 651 (1978).
- [27] P. Mitchell, J. A. Baxter, J. Comer, and P. J. Hicks, *J. Phys. B: At., Mol. Opt. Phys.* **13**, 4481 (1980).
- [28] K. Jorgensen, N. Andersen, and J. O. Olsen, *J. Phys. B: At., Mol. Opt. Phys.* **11**, 3951 (1978).
- [29] J. A. Simpson, G. E. Chamberlain, and S. R. Mielczarek, *Phys. Rev.* **139**, A1039 (1965).
- [30] M. E. Rudd, T. Jorgensen, and D. J. Volz, *Phys. Rev.* **151**, 28 (1966).
- [31] G. Gerber, R. Morgenstern, and A. Niehaus, *Phys. Rev. Lett.* **23**, 511 (1969).
- [32] C. E. Brion and L. A. R. Olsen, *J. Phys. B: At., Mol. Opt. Phys.* **3**, 1020 (1970).
- [33] L. Sanche and G. J. Schulz, *Phys. Rev. A* **5**, 1672 (1972).
- [34] A. Crowe, J. A. Preston, and J. W. McConkey, *J. Chem. Phys.* **57**, 1620 (1972).
- [35] J. W. McConkey and J. A. Preston, *J. Phys. B: At., Mol. Opt. Phys.* **6**, L138 (1973).
- [36] R. J. Tweed, F. Gelebart, and J. Peresse, *J. Phys. B: At., Mol. Opt. Phys.* **9**, 2643 (1976).
- [37] W. F. Chan, G. Cooper, X. Guo, G. R. Burton, and C. E. Brion, *Phys. Rev. A* **46**, 149 (1992).
- [38] S. L. Wu, Z. P. Zhong, R. F. Feng, S. L. Xing, B. X. Yang, and K. Z. Xu, *Phys. Rev. A* **51**, 4494 (1995).
- [39] L. F. Zhu, H. D. Cheng, X. J. Liu, P. Tian, Z. S. Yuan, W. B. Li, and K. Z. Xu, *Chin. Phys. Lett.* **20**, 1718 (2003).
- [40] J. J. Jureta, B. P. Marinkovic, and L. Avaldi, *Eur. Phys. J. D* **70**, 199 (2016).
- [41] P. G. Burke and K. T. Taylor, *J. Phys. B: At., Mol. Opt. Phys.* **8**, 2620 (1975).
- [42] X. M. Tong and T. Watanabe, *Phys. Rev. A* **76**, 042715 (2007).
- [43] T. Watanabe, A. T. Domondon, and X. M. Tong, *Phys. Rev. A* **80**, 042709 (2009).
- [44] K. Z. Xu, R. F. Feng, S. L. Wu, Q. Ji, X. J. Zhang, Z. P. Zhong, and Y. Zheng, *Phys. Rev. A* **53**, 3081 (1996).
- [45] X. J. Liu, L. F. Zhu, X. M. Jiang, Z. S. Yuan, B. Cai, X. J. Chen, and K. Z. Xu, *Rev. Sci. Instrum.* **72**, 3357 (2001).
- [46] T. Chen, Y. W. Liu, Y. C. Xu, and L. F. Zhu, *J. Phys. B: At., Mol. Opt. Phys.* **53**, 085201 (2020).
- [47] Z. P. Zhong, R. F. Feng, K. Z. Xu, S. L. Wu, L. F. Zhu, X. J. Zhang, Q. Ji, and Q. C. Shi, *Phys. Rev. A* **55**, 1799 (1997).
- [48] Y. W. Liu, L. Q. Xu, D. D. Ni, X. Xu, X. C. Huang, and L. F. Zhu, *J. Geophys. Res. Space Phys.*, **122**, 3459 (2017).
- [49] H. Bethe, *Ann. Phys.* **397**, 325 (1930).
- [50] H. Bethe, *Z. Phys.* **76**, 293 (1932).
- [51] M. Inokuti, *Rev. Mod. Phys.* **43**, 297 (1971).